Available online at www.sciencedirect.com
ScienceDirect
Acta Materialia 58 (2010) 1679–1687
Acta MATERIALIA
www.elsevier.com/locate/actamat

The effect of film thickness on the failure strain of polymer-supported metal films

Nanshu Lu, Zhigang Suo, Joost J. Vlassak *

School of Engineering and Applied Sciences, Harvard University, Cambridge, MA 02138, USA

Received 4 September 2009; received in revised form 5 November 2009; accepted 7 November 2009
Available online 16 December 2009

Abstract

We perform uniaxial tensile tests on polyimide-supported copper films with a strong (1 1 1) fiber texture and with thicknesses varying from 50 nm to 1 μm. Films with thicknesses below 200 nm fail by intergranular fracture at elongations of only a few percent. Thicker films rupture by ductile transgranular fracture and local debonding from the substrate. The failure strain for transgranular fracture exhibits a maximum for film thicknesses around 500 nm. The transgranular failure mechanism is elucidated by performing finite element simulations that incorporate a cohesive zone along the film/substrate interface. As the film thickness increases from 200 to 500 nm, a decrease in the yield stress of the film makes it more difficult for the film to debond from the substrate, thus increasing the failure strain. As the thickness increases beyond 500 nm, however, the fraction of (1 0 0) grains in the (1 1 1)-textured films increases. On deformation, necking and debonding initiate at the (1 0 0) grains, leading to a reduction in the failure strain of the films.

Keywords: Metal films; Failure strain; Thickness; Yield strength; Texture

1. Introduction

Flexible electronic devices integrate diverse inorganic materials such as semiconductors, metals and ceramics on a polymer substrate. Benefits such as low weight, ruggedness, low costs, large area and ease of integration promise to open doors to new applications in areas where conventional electronics have not been effective. Applications of flexible electronics include paper-like electronic displays [1], conformable electronic textiles [2], rollable solar cells [3] and flexible RFID tags [4]. Flexible electronic devices are usually made as organic/inorganic hybrids. One architecture uses metallic films that are patterned into interconnects to link isolated functional ceramic islands supported by a deformable polymer substrate [5–8]. When such a structure is stretched or bent, the polymer substrate carries most of the deformation while the ceramic islands experience only small strains. As a result, the whole system can sustain large applied deformations without rupturing the electronic components. In this architecture, the metallic interconnects between the islands have to deform along with the underlying substrate. Failure of these interconnects results in a loss of electrical connectivity between the islands. In this paper, we investigate the fundamental mechanisms that limit the strain of metal films attached to polymer substrates.

Freestanding metal films stretched in tension are often reported to rupture at small strains. When stretched, a freestanding film of a ductile metal ruptures by forming a neck within a narrow region. Although the strain within the neck is large, the strain elsewhere in the film is small. Because thin-film samples often have very large length-to-thickness ratios, the net elongation of the freestanding film upon rupture is small, typically less than a few percent [9–13].

For a metal film that is well bonded to a polymer substrate, finite element simulations have shown that the polymer substrate can suppress necking in the metal film, so that the film can elongate indefinitely, limited only by rupture of the polymer substrate [14,15]. Experimentally, however,

* Corresponding author.
E-mail address: vlassak@esag.deas.harvard.edu (J.J. Vlassak).

1359-6454/$36.00
doi:10.1016/j.actamat.2009.11.010

most polymer-supported thin metal films rupture at small elongations (<10%) [16–23], even though elongations as high as 20% have been reported in a few cases [24–26]. Our recent experiments have achieved elongations over 50% of polyimide-bonded Cu films without detectable fracture [27]. We have demonstrated that good adhesion between film and substrate is critical to achieving large failure strains, an observation that is consistent with both theoretical predictions [15] and a previous experimental investigation [22].

Strong adhesion is not the only condition required to achieve large failure strains. It is also important to ensure that deformation occurs as uniformly as possible. Another set of experiments showed that sputtered Cu films rupture at much smaller strains in their as-deposited state as compared to annealed films [28]. Without thermal treatment, the microstructure of as-deposited Cu films is unstable during deformation and room-temperature grain growth is observed under mechanical loading. Eventually, the films fail by ductile necking as a result of concurrent grain growth, strain localization at large grains and film debonding from the substrate.

In this paper, we present a comprehensive experimental study of the effect of film thickness on the failure strain of annealed Cu coatings supported by polyimide substrates. The yield strength and crystallographic texture of the film are found to have a significant impact on the failure strain. These effects are further elucidated by modelling ductile fracture of the coatings using the finite element method. The paper is organized as follows. Section 2 describes the experimental setup and procedures. Experimental results including resistance–elongation measurements and sample micrographs are provided in Section 3. The finite element simulations are described in Section 4. Final conclusions are given in Section 5.

2. Experimental detail

The polymer substrates used in this study were 12.7 μm polyimide foils (Kapton 50HN® by DuPont, Circleville, OH). Immediately prior to the deposition of metal films, the substrates were ultrasonically cleaned with acetone and methanol. The substrates were then covered by a shadow mask with seven 5×50 mm^2 rectangular windows and placed inside the chamber of a direct-current (DC) magnetron sputter-deposition system with a base pressure better than 1×10^{-7} Torr. After sputter cleaning for 5 min with an Ar plasma at a radio-frequency power of 24 W and a pressure of 2×10^{-2} Torr, a Cu layer was deposited onto the substrates through the windows in the shadow mask. The deposition was performed using a 50.8 mm Cu target at a DC power of 200 W and a working gas (Ar) pressure of 5×10^{-3} Torr. The nominal target–substrate distance was 100 mm and the corresponding deposition rate was 0.39 nm s^{-1}. The thickness of the film was controlled by varying the deposition time. These deposition conditions are similar to those used in Refs. [27,28]. Immediately after deposition, the Cu films were annealed at 150 °C for 1 h. Annealed specimens were removed from the vacuum chamber after 12 h to allow them to cool down prior to breaking vacuum. Additional annealing under these conditions did not further increase the grain size.

The microstructure of the films was characterized by means of focused ion beam (FIB) imaging in a Zeiss NVision40 Dual-Beam FIB/SEM (Carl Zeiss Inc. Thornwood, NY). Fig. 1a shows typical FIB images for the 50 nm and 1 μm films, illustrating the change in grain size with film thickness. The crystallographic texture of the films was measured using electron backscattered diffraction (EBSD). The EBSD measurements were performed in a Zeiss Supra55VP SEM. Fig. 1b shows orientation maps for the 500 nm and 1 μm films respectively. Grains marked blue are oriented with the (1 1 1) plane parallel to the surface, grains in red[1] are (1 0 0) oriented and grains labelled green possess a (1 0 1) orientation. Both films show a strong (1 1 1) texture, but the 1 μm film contains more (1 0 0) grains than the 500 nm film, as also observed in similar polyimide-supported Cu films [29]. The volume fractions of (1 0 0) grains were estimated from at least five EBSD images for each film thickness and are listed in Table 1. The average grain size was determined by the intercept method with twins counted as separate grains, the same method as used in Ref. [30]. The relation between film thickness and grain size is shown in Fig. 1c. The volume fraction of (1 0 0) grains and grain size are tabulated in Table 1 for further reference.

Rectangular tensile test specimens with a width of 5 mm were cut from the metal-coated substrates using a razor blade. The specimen gauge length was $L_0 = 30$ mm. The specimens were then subject to uniaxial tension using an Instron 3342 tensile tester. All tests were performed at room temperature at a constant strain rate of 3.3×10^{-4} s^{-1}. During tensile testing, the electrical resistance of the films was measured in situ using a Keithley 2000 multimeter in a four-point measurement setup. We used the Zeiss NVision40 Dual-Beam FIB/SEM to examine specimens stretched to different elongations after unloading. At least six samples were tested for each thickness.

3. Results

3.1. In situ resistance measurements and failure strain determination

Fig. 2a shows typical experimental resistance–elongation curves for films with thicknesses ranging from 50 nm to 1 μm, along with the theoretical curve

$$R/R_0 = (L/L_0)^2 \quad (1)$$

which holds as long as there are no resistivity or volume changes during the experiment. We define the failure strain,

[1] For interpretation of color in Figs. 1, 2 and 4–8, the reader is referred to the web version of this article.

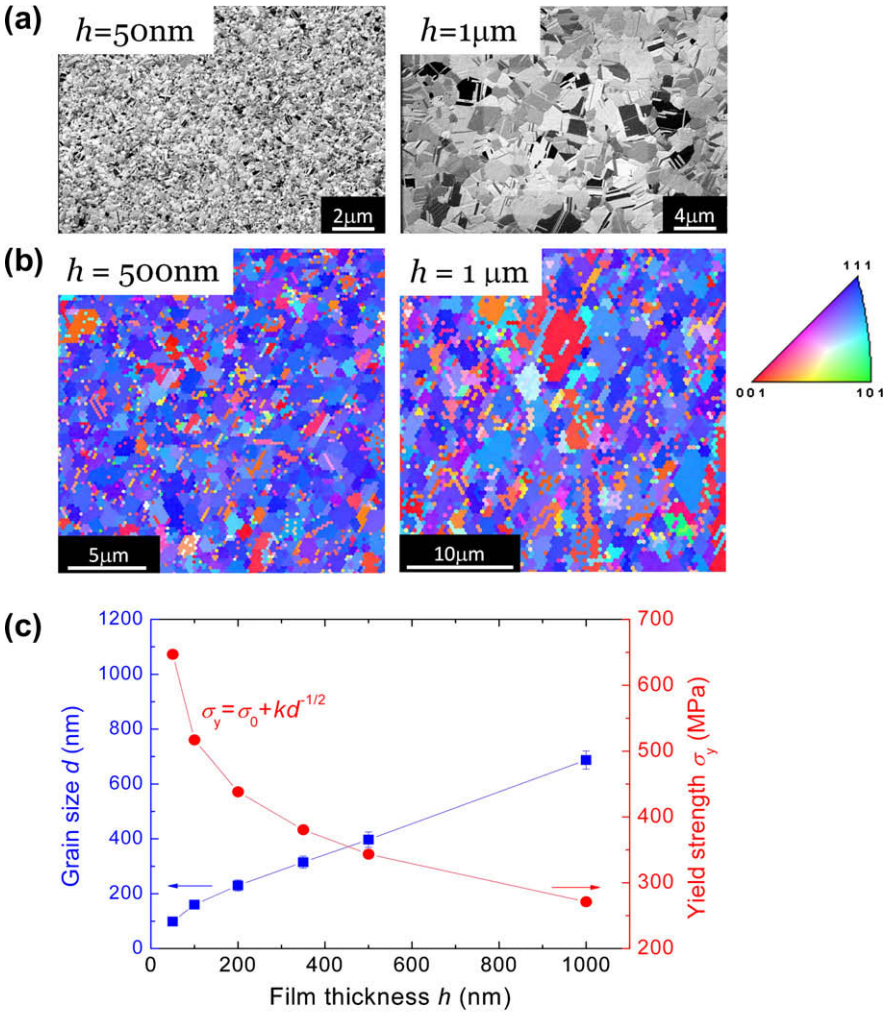

Fig. 1. (a) Focused ion beam images of films with various thicknesses. (b) Crystal orientation maps for the 500 nm and 1 μm films. (c) Grain size (squares) and yield strength (dots) as a function of film thickness. Yield strengths are calculated from the Hall–Petch relation $\sigma_y = \sigma_0 + kd^{-1/2}$ using the coefficients $\sigma_0 = 42$ MPa and $k = 6008.3$ MPa nm$^{1/2}$ from Ref. [30].

Table 1
Microstructure and strain-to-rupture of films.

Thickness, h (nm)	$f_{(100)}$ (%)[a]	Grain size, d (mm)[a]	Yield strength, σ_y (MPa)	Strain-to-failure (experimental) (%)[b]	Strain-to-failure (FEM) (%)
50	4.3 ± 0.4	98.6 ± 8	647	4.5 ± 1	11
100	4.1 ± 1	162.7 ± 15	513	8.3 ± 2.2	19
200	4.1 ± 0.5	231.3 ± 20	437	17.8 ± 0.1	32
350	4 ± 0.2	315.8 ± 22	380	24.4 ± 1.5	45.6
500	4.3 ± 0.5	397.2 ± 28	343	54.2 ± 0.5	54
1000	7.4 ± 0.2	687.4 ± 33	271	39.8 ± 0.5	10.6

[a] Errors denote the standard deviation for five different EBSD micrographs.
[b] Errors denote the standard deviation for at least three different samples of a given thickness.

ε_r, as the strain at which the experimental curve deviates from the theoretical curve by 0.05. We have verified that for our films this strain indeed corresponds to the strain at which cracks start to initiate on a large scale [27,28]. With this definition, we can plot the failure strain as a function of film thickness in Fig. 2b. It is evident from Fig. 2a and b that the 500 nm films have the highest failure strain, approximately 54%, among the six sets of samples that were tested. The 1 μm films fail at slightly smaller strains. As the film thickness decreases below 500 nm, the failure strain decreases rapidly; the 50 nm films rupture at strains not greater than 5%. Representative SEM micrographs of films after a 30% elongation are shown in Fig. 2c. No cracks can be found in the 1 μm or 500 nm films and their resistances do not deviate from Eq. (2), as shown in Fig. 2a. By contrast, isolated microcracks can be found in the 350

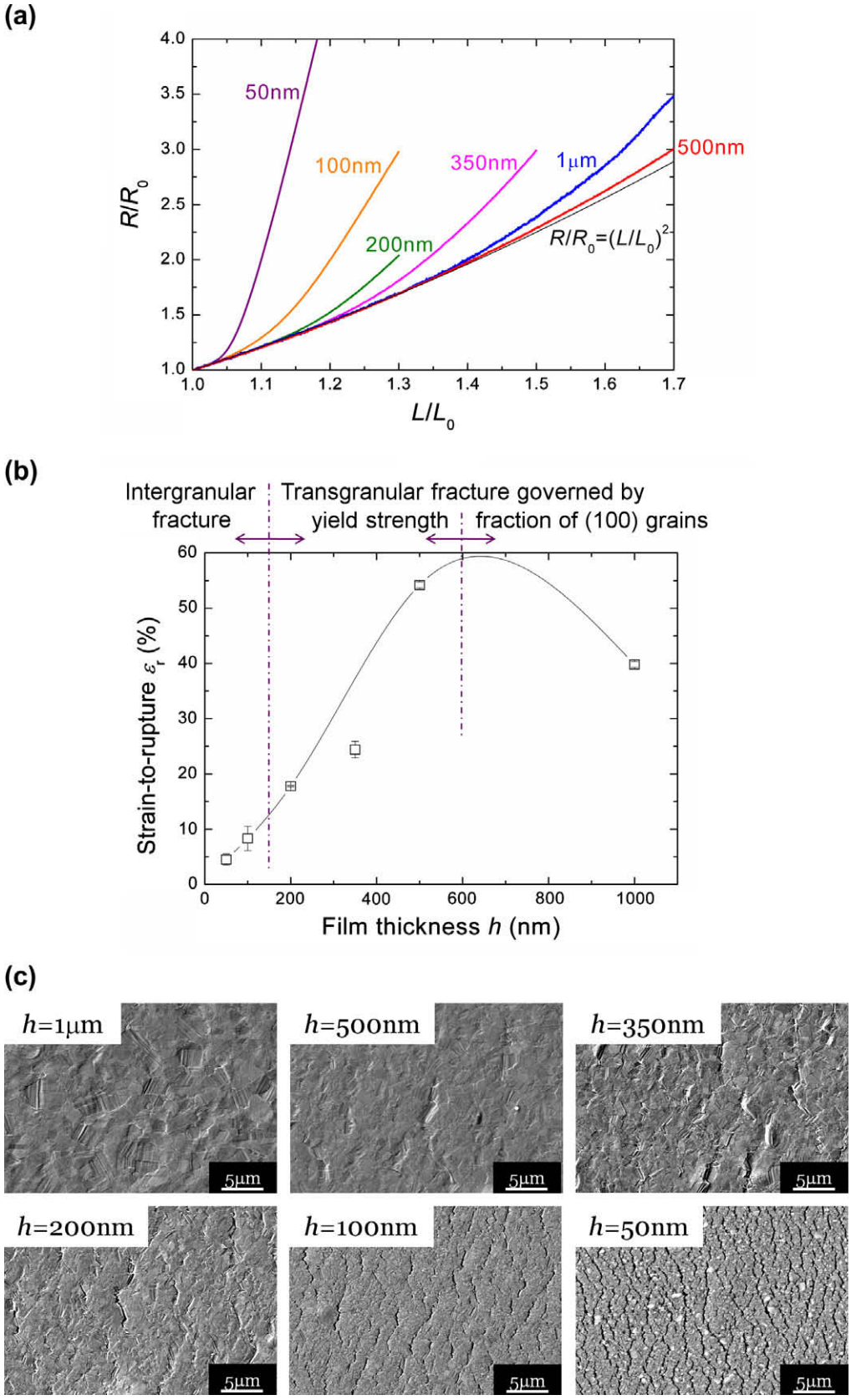

Fig. 2. (a) Experimental resistance as a function of uniaxial film elongation, along with the theoretical resistance assuming volume conservation and no resistivity change during deformation; (b) failure strain as a function of film thickness; (c) micrographs of films stretched by 30%. Loading is along horizontal direction for all micrographs.

and 200 nm films and moderate offsets of their resistances from Eq. (2) are observed in Fig. 2a. As the film thickness decreases below 200 nm, the crack density increases markedly and the cracks are interconnected, explaining the steep rise in film resistance observed in Fig. 2a. In the following, we will elucidate the mechanisms that are responsible for the observed variation in the failure strains.

3.2. Transgranular vs. intergranular fracture

Films with thicknesses of 200 nm or greater can accommodate large strains without forming cracks. Fig. 3 shows plan-view and cross-sectional FIB micrographs of 1 μm, 500 nm and 200 nm films deformed to elongations of 70%, 70% and 40%, respectively. Abundant slip traces of dislocations can be observed in Fig. 3a, c and e, indicating that all three films have experienced extensive plastic deformation. When 1 μm and 500 nm films are stretched 70%, Fig. 3a and c and many other micrographs like them show that only isolated transgranular cracks associated with one or two grains can be detected. The cross-sectional images (Fig. 3b and d) reveal that the films rupture by a ductile mechanism, in which debonding and necking coevolve. This observation is consistent with previous computational [14,15] and experimental [27] studies. The 200 nm films show more extensive cracking at 40% strain (Fig. 3e), but failure still occurs through ductile transgranular fracture. A cross-sectional view (Fig. 3f) at the site of one of the microcracks shows that the film ruptures by debonding from the substrate and by necking down to a knife-edge. The micrographs in Fig. 3 are representative of all films with thicknesses between 1 μm and 200 nm. We conclude that there is no change in failure mode as the film thickness decreases from 1 μm to 200 nm.

By contrast, a different failure mode is found in films with thicknesses equal to or smaller than 100 nm. Fig. 4 shows top and cross-sectional images of 100 and 50 nm films strained to 40% and 30%, respectively. As opposed to the transgranular cracks observed in the submicron films, Fig. 4a and c shows irregularly notched crack paths that follow the grain boundaries, indicating intergranular fracture. The intergranular cracks are often interconnected, forming long transverse cracks that are particularly detrimental to the conductivity of the film. Metal films in this thickness range have a large yield strength and are difficult to deform plastically because of dimensional constraints on dislocation activity [31]. The high level of stress supported by these films evidently triggers grain boundary decohesion before ductile failure occurs. Since grain boundary decohesion is a relatively brittle fracture mechanism compared to necking, the total elongation at failure is small. Furthermore, no debonding is required to accommodate local displacements because grain boundary decohesion does not involve large local elongations. Consequently, no necking or debonding is observed in Fig. 4b and d.

3.3. Preferred transgranular fracture at (1 0 0) grains

As illustrated in Fig. 2b, the 1 μm films have a smaller failure strain than the 500 nm films. It is evident from Fig. 3a–d that there is little difference between the morphologies of the two films after 70% strain. In both cases, only isolated transgranular cracks associated with one or a few grains are found. The reduced strain-to-failure of 1 μm films is explained, however, by noting that the transgranular cracks are associated predominantly with (1 0 0) oriented grains.

It is well known that the crystallographic texture of a film varies with film thickness as a result of a trade-off between interfacial energy and strain energy [32]. In particular, thin films of face-centered cubic (fcc) metals tend to have a strong (1 1 1) texture, while thicker films also have a (1 0 0) texture component that increases with film thickness

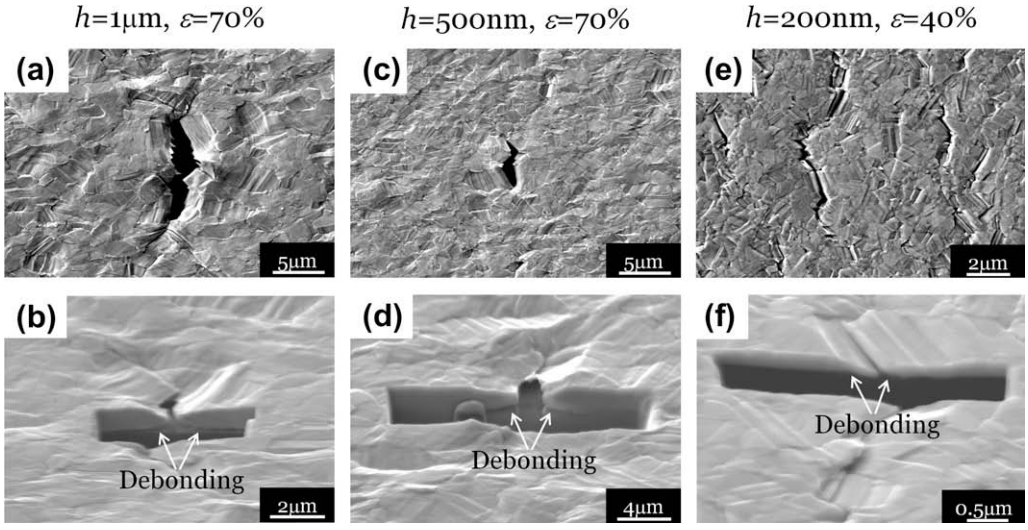

Fig. 3. Surface and cross-sectional views of 1 μm, 500 nm and 200 nm films stretched by 70%, 70% and 40%, respectively. These images are representative of all films with thicknesses between 200 nm and 1 μm. Loading is along horizontal direction for all micrographs.

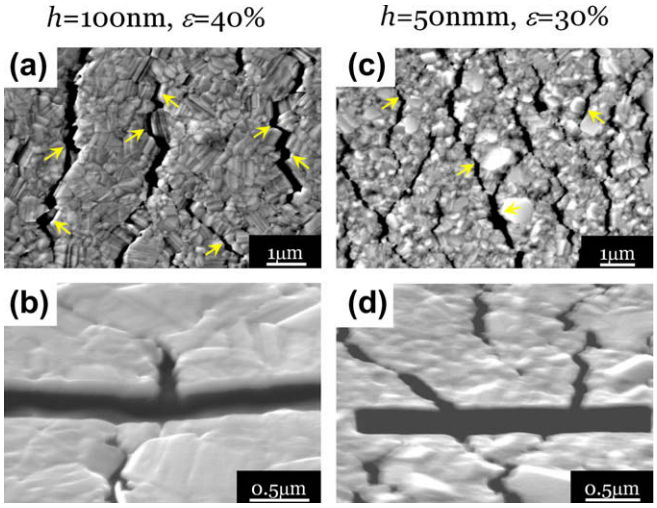

Fig. 4. Surface and cross-sectional views of 100 and 50 nm films stretched by 40% and 30%, respectively. Loading is along the horizontal direction for all micrographs.

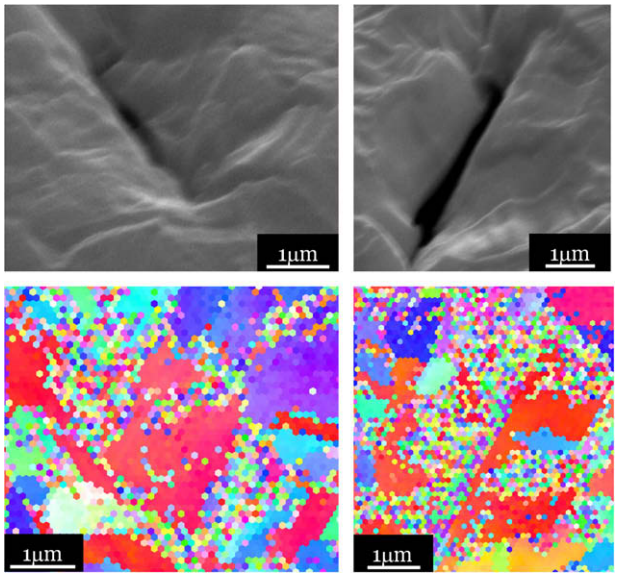

Fig. 5. Representative micrographs and corresponding crystal orientation maps of regions with cracks in a 1 μm film deformed by 70%. The (1 0 0) orientation is marked by red. (For interpretation of the references to color in this figure legend, the reader is referred to the web version of this paper.)

[29,33–38]. Orientation maps of 500 nm and 1 μm films obtained by EBSD are shown in Fig. 1b. Grains with a (1 0 0) orientation have a much lower flow stress than (1 1 1) grains. This is evident, for instance, if one calculates the Taylor factor for an fcc film with a (1 1 1) and a (1 0 0) fiber texture subjected to uniaxial deformation, yielding a flow stress ratio, $\sigma_{(111)}/\sigma_{(100)}$, as large as 2.41. Calculation of the corresponding Schmidt factors also leads to the conclusion that the (1 0 0) grains have a lower flow stress than (1 1 1) grains [38]. Consequently, (1 0 0) grains in a (1 1 1) textured film can be regarded as soft inclusions embedded in a hard matrix. Because the inclusion has a lower flow stress and deforms more easily, it becomes a preferential site for strain localization and necking. Large local elongation triggers simultaneous debonding and ultimately evolves into transgranular fracture. Once a microcrack forms, stress concentrations at the crack tips may cause fracture in adjacent grains. Since the (1 0 0) grains are dispersed in the film, only isolated transgranular cracks associated with one or two grains are observed as illustrated in Fig. 3a and c. Given that the 1 μm film contains a larger fraction of (1 0 0) grains than the 500 nm film, this mechanism provides a simple explanation why the strain-to-failure decreases with film thickness above 500 nm.

To confirm that fracture indeed occurs predominantly at (1 0 0) grains, we performed EBSD scans of regions containing microcracks in deformed 1 μm films. Fig. 5 shows two of the many examples where transgranular cracks are associated with at least one (1 0 0) grain. Due to extensive plastic deformation and grain rotation, the EBSD indexing rate is low and only partial grains can be identified. Even so, a statistical study of the EBSD images of microcracks in six samples deformed by 70% shows that the volume fraction of (1 0 0) grains in images that contain a microcrack is at least 17%. This volume fraction is significantly larger than the overall volume fraction of (1 0 0) grains, which is only 7%.

4. Finite element simulations

To provide additional insight into the ductile failure mode, we perform a finite element analysis of the film/substrate system. We use a finite element model similar to the model described in Refs. [14,15]. Fig. 6a depicts a two-dimensional plane-strain model of a blanket metal film on a polymer substrate under uniaxial tension. The film thickness h is varied over the range of the experimental values used in this study and the substrate thickness H is fixed at 12.7 μm, the thickness of the Kapton 50HN substrate. The length of the film in the model is set to $L = 80$ μm. Both materials are modeled as homogeneous isotropic elastic–plastic solids with a uniaxial true stress–true strain relationship given by

$$\sigma = \begin{cases} E\varepsilon, \varepsilon \leqslant \sigma_y/E \\ \sigma_y\left(\frac{\varepsilon}{\sigma_y/E}\right)^N, \varepsilon > \sigma_y/E \end{cases} \quad (2)$$

where E is Young's modulus, σ_y is the yield stress and N is the hardening exponent. The mechanical properties used in the finite element calculations for Cu and Kapton are listed in Table 2. The yield strength of the Cu films is estimated from the grain size using the Hall–Petch relationship

$$\sigma_y = \sigma_0 + kd^{-1/2} \quad (3)$$

and is listed as a function of film thickness in Table 1. Values of $\sigma_0 = 42$ MPa and $k = 6008$ MPa nm$^{1/2}$ have been obtained from bulge test measurements on unpassivated Cu films with similar thicknesses deposited previously in the same deposition system [30]. The yield strength is plotted as a function of film thickness in Fig. 1c. The Kapton yield strength and its Young's modulus are measured directly in uniaxial tensile tests on bare Kapton substrates; the other

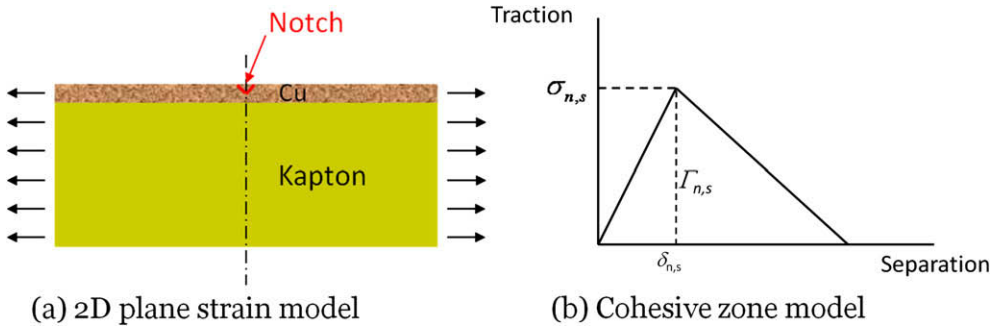

Fig. 6. (a) Two-dimensional plane-strain model of a polyimide-bonded copper thin film subjected to uniaxial stretching. A small notch is introduced as an imperfection at the center of the film. Only the right half of the structure is modelled because of the symmetry. (b) Constitutive law of the cohesive zone at the film/substrate interface.

parameters are typical values for this material. To model the coevolution of necking and film/substrate debonding, a cohesive zone that consists of an array of nonlinear springs with the traction–separation relation shown in Fig. 6b is applied at the interface. The parameters σ_n and σ_s are the normal and the shear strengths; δ_n and δ_s refer to the normal and the shear separations; the areas under the traction–separation curves are the respective toughnesses, denoted by Γ_n and Γ_s. We assume the same interfacial parameters for all simulations: $\sigma_n = \sigma_s = 150$ MPa, $\delta_n = \delta_s = 1.5$ nm and $\Gamma_n = \Gamma_s = 5$ J m^{-2}. These values are representative of a metal/polymer interface, and are chosen to fit the experimental results.

Because of symmetry, only the right half of the system needs to be modeled. The appropriate symmetry boundary conditions are applied along the symmetry axis, and the bottom point on this axis is fixed in space. The right side of the model is subjected to a uniform horizontal displacement u. The engineering strain is given by $\varepsilon_{app} = 2u/L$. A small notch with a depth of $0.02h$ and a width of $0.2h$ is introduced on the film surface at the center of the model to serve as an imperfection where the neck can nucleate. Both the film and the substrate are meshed by four-point quadrilateral plane-strain elements. The cohesive layer consists of two-dimensional cohesive elements that share nodes with film and substrate. As the simulation carries on, coevolution of necking and debonding can be observed in the vicinity of the notch. We define the failure strain as the strain at which the local film thickness decreases to one tenth of its original thickness. Since the FEM model does not contain any grain boundaries, only films that fail by ductile transgranular fracture are modeled. In the following, we first examine the effect of film thickness by decoupling geometry and yield strength effects. Then we examine the effect of crystallographic texture. A survey of all simulation results is shown in Fig. 7.

Table 2
Material properties used in FEM simulations.

Material	Young's modulus, E (GPa)	Poisson's ratio, v	Yield strength, σ_y (MPa)	Hardening exponent, N
Kapton	2.34	0.34	24	0.625
Homogenized Cu	130	0.36		
(1 0 0) Cu	93	0.19	As labeled in Fig. 8	0.02
(1 1 1) Cu	130	0.50		

4.1. Effect of geometry

To evaluate any geometric effects associated with changing the film thickness, we vary the film thickness in the FEM simulations without changing the yield strength of the films. The strains-to-failure are plotted as triangles in Fig. 7; evidently the strain-to-failure is very nearly independent of film thickness. Fig. 8a–c shows the corresponding deformed configurations; it is clear that there is no obvious change in failure mode. This can be understood in terms of the characteristic length scales of the film/substrate system. First, the length scales associated with the traction–separation law for the cohesive zone, $\delta_n = \delta_s = 1.5$ nm, are at least two orders of magnitude smaller than the film thicknesses considered in this study. Second, the substrate is at least one order of magnitude thicker than the films. As a result, relatively small changes in film thickness do not affect the failure strain significantly.

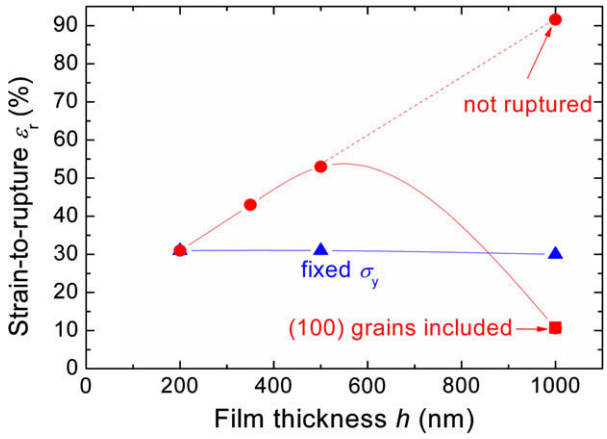

Fig. 7. Failure strain vs. film thickness obtained from FEM simulations.

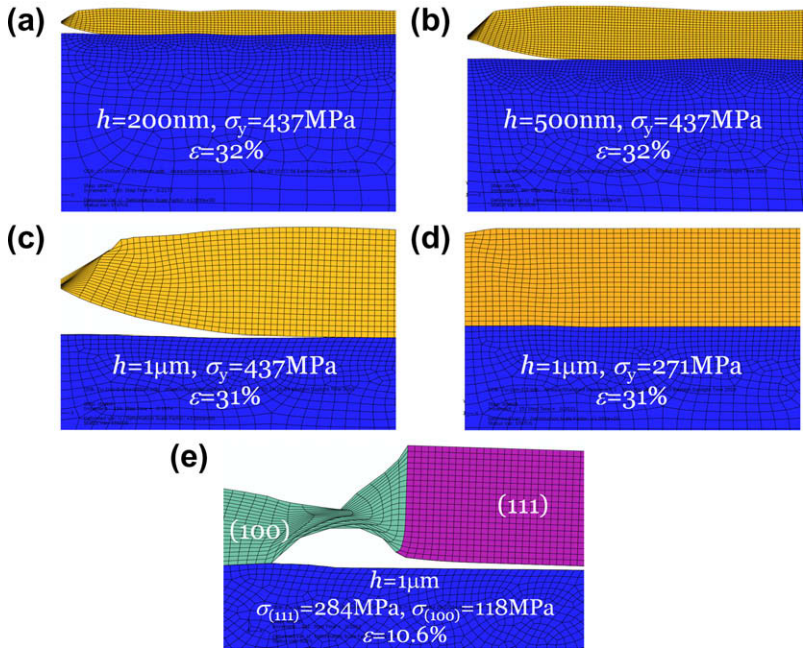

Fig. 8. Deformed configurations of metal films on polymer substrates obtained from FEM simulations. Only the right half of Fig. 6a is modeled. For clarity, only part of the substrate is shown. (a–c) Films with fixed yield strength and varying thickness. (d) A film with reduced yield strength. (e) A 1 μm film with a (1 0 0) grain.

4.2. Effect of yield strength

Fig. 1c shows that the yield strength of the Cu films decreases with increasing thickness. To evaluate the effect of the yield strength on the failure strain of the films, Cu films are modeled with the yield strengths as listed in Table 1. The simulation results are plotted as dots in Fig. 7. The failure strain now increases with increasing film thickness, i.e. with decreasing yield strength. Evidently the yield strength of the 1 μm film is so low that it does not fail. This trend is readily understood. When the yield strength of the film is large compared to the interfacial strength, the film can exert large tractions on the interface, making it easier to initiate debonding from the substrate. Once the film is debonded, the substrate cannot suppress strain localization anymore and the film fails by the coevolution of necking and debonding. Increasing the yield strength of the films clearly facilitates this process and decreases the failure strain. If the film yield strength is too low, however, there is insufficient driving force to initiate delamination and the film can be stretched without ever debonding or necking. Fig. 8c and d illustrates this mechanism. For the same film thickness and imposed strain, the film with the larger yield strength has a much larger region of delamination. Since debonding and necking facilitate each other, the stronger film will rupture at a smaller elongation.

4.3. Effect of film texture

The FEM model in the previous section assumes uniform properties for the Cu film; it does not capture any texture effects. Thus it is not surprising that the behavior of the 1 μm is not simulated correctly. We now investigate the effect of texture on the failure strain by simulating a soft (1 0 0) grain embedded in a 1 μm film with a (1 1 1) fiber texture.

The size of the (1 0 0) inclusion is chosen such that the volume fraction of (1 0 0) grains in the FEM model is same as in the experiments. The elastic properties are calculated from the Cu single-crystal constants, $c_{11} = 168.4$ GPa, $c_{12} = 121.4$ GPa and $c_{44} = 75.4$ GPa [39], by spatially averaging the properties in the (1 0 0) and (1 1 1) planes, yielding $E_{(100)} = 93$ GPa, $\nu_{(100)} = 0.19$, $E_{(111)} = 130$ GPa and $\nu_{(111)} = 0.50$. The yield strengths are taken such that their volume average is equal to the yield strengths listed in Table 1 and their ratio is equal to the ratio of the in-plane averaged Taylor factors, $\sigma_{(111)}/\sigma_{(100)} = 2.41$. The failure strain is plotted in Fig. 7 with the label "(1 0 0) grains included". Compared to the homogeneous 1 μm film, this film exhibits a much reduced failure strain. As illustrated in Fig. 8e, this reduction is caused by an almost-immediate strain localization in the soft inclusion. It should be noted that the failure strain in the FEM model is much smaller than that observed experimentally because of the two-dimensional nature of the FEM model: the FEM model assumes a strip of soft grains across the width of the film, rather than dispersed (1 0 0) grains as observed in the experiments (Fig. 1b).

5. Summary

We have carried out uniaxial tensile experiments on polyimide-supported copper films with thicknesses varying from 50 nm to 1 μm and a (1 1 1) fiber texture. The

experimental failure strains first rise with film thickness, reach a maximum for film thicknesses around 500 nm and then decrease again. Several factors are responsible for this behavior. Films with thicknesses less than 200 nm fail at very low strains as a result of intergranular fracture. For thicker films, the failure mode switches to transgranular fracture in a process that involves both strain localization and debonding. As the yield strength decreases with increasing film thickness, it becomes increasingly difficult to debond the film from the substrate and the failure strain increases. Eventually, a (1 0 0) texture component develops in the films, leading to strain localization and fracture at the softer (1 0 0) grains. This mechanism results in a lowering of the failure strain. Our observations suggest that the failure strain of a metal film on a polymer substrate can be maximized by ensuring good adhesion between film and substrate, a uniform crystallographic texture, and a large grain size to lower the yield strength.

Acknowledgements

The work presented in this paper was supported by the National Science Foundation (NSF) under Grant CMS-0556169, and by the Materials Research Science and Engineering Center (MRSEC) at Harvard University. It was performed in part at the Center for Nanoscale Systems (CNS), a member of the National Nanotechnology Infrastructure Network (NNIN), which is supported by the National Science Foundation under NSF Award No. ECS-0335765. CNS is part of the Faculty of Arts and Sciences at Harvard University. The authors thank David Mooney for use of the Instron tensile tester.

References

[1] Rogers JA, Bao Z, Baldwin K, Dodabalapur A, Crone B, Raju VR, et al. Proc Natl Acad Sci USA 2001;98:4835.
[2] Bonderover E, Wagner S. IEEE Electron Device Lett 2004;25:295.
[3] Brabec CJ. Sol Energy Mater Sol Cells 2004;83:273.
[4] Miller P. SEL and TDK Announce World's "First" Flexible RFID; 2006.
[5] Ko HC, Stoykovich MP, Song JZ, Malyarchuk V, Choi WM, Yu CJ, et al. Nature 2008;454:748.
[6] Bhattacharya R, Wagner S, Tung YJ, Esler JR, Hack M. Proc IEEE 2005;93:1273.
[7] Hsu PI, Bhattacharya R, Gleskova H, Huang M, Xi Z, Suo Z, et al. Appl Phys Lett 2002;81:1723.
[8] Sun JY, Lu N, Yoon J, Oh KH, Suo Z, Vlassak JJ. J Mater Res 2009;24:3338.
[9] Keller RR, Phelps JM, Read DT. Mater Sci Eng, A 1996;214:42.
[10] Huang H, Spaepen F. Acta Mater 2000;48:3261.
[11] Xiang Y, Chen X, Vlassak JJ. Mater Res Symp Proc 2002;659:L4.9.
[12] Espinosa HD, Prorok BC, Fischer M. J Mech Phys Solids 2003;51:47.
[13] Lee HJ, Zhang P, Bravman JC. J Appl Phys 2003;93:1443.
[14] Li T, Huang ZY, Xi ZC, Lacour SP, Wagner S, Suo Z. Mech Mater 2005;37:261.
[15] Li T, Suo Z. Int J Solids Struct 2006;44:1696.
[16] Chui SL, Leu J, Ho PS. J Appl Phys 1994;76:5136.
[17] Kraft O, Hommel M, Arzt E. Mater Sci Eng 2000;A288:209.
[18] Hommel M, Kraft O. Acta Mater 2001;49:3935.
[19] Alaca BE, Saif MTA, Sehitoglu H. Acta Mater 2002;50:1197.
[20] Lacour SP, Wagner S, Huang Z, Suo Z. Appl Phys Lett 2003;82:2404.
[21] Yu DYW, Spaepen F. J Appl Phys 2003;95:2991.
[22] Xiang Y, Li T, Suo Z, Vlassak JJ. Appl Phys Lett 2005;87:161910.
[23] Niu RM, Liu G, Wang C, Zhang G, Ding XD, Sun J. Appl Phys Lett 2007:90.
[24] Kang YS. Microstructure and strengthening mechanisms in aluminum thin films on polyimide film, Ph.D. Thesis, University of Texas at Austin; 1996.
[25] Macionczyk F, Bruckner W. J Appl Phys 1999;86:4922.
[26] Gruber P, Böhm J, Wanner A, Sauter L, Spolenak R, Arzt E. Mater Res Soc Symp Proc 2003;821:P2.7.
[27] Lu N, Wang X, Suo Z, Vlassak JJ. Appl Phys Lett 2007;91:221909.
[28] Lu N, Wang X, Suo Z, Vlassak JJ. J Mater Res 2009;24:379.
[29] Sonnweber-Ribica P, Gruberb P, Dehmc G, Arzt E. Acta Mater 2006;54:3863.
[30] Xiang Y, Vlassak JJ. Acta Mater 2006;54:5449.
[31] Meyers MA, Mishra A, Benson DJ. Prog Mater Sci 2006;51:427.
[32] Thompson CV. Annu Rev Mater Sci 2000;30:159.
[33] Harper JME, Gupta J, Smith DA, Chang JW, Holloway KL, Cabral C, et al. Appl Phys Lett 1994;65:177.
[34] Zielinski EM, Vinci RP, Bravman JC. J Appl Phys 1994;76:4516.
[35] Perez-Prado MT, Vlassak JJ. Scripta Mater 2002;47:817.
[36] Perez-Prado MT, Vlassak JJ. Textures Mater 2002;408:1639.
[37] Zhang JM, Xu KW, Ji V. Appl Surf Sci 2002;187(PII):S0169.
[38] Baker SP, Kretschmann A, Arzt E. Acta Mater 2001;49:2145.
[39] Simmons G, Wang H. Single crystal elastic constants and calculated aggregate properties. 2nd edn. Cambridge (MA): MIT Press; 1971.